RIVER FLOW

Anthropogenic climate change has influenced global river flow seasonality

Hong Wang[1,2], Junguo Liu[1,3,4]*, Megan Klaar[2], Aifang Chen[1], Lukas Gudmundsson[5], Joseph Holden[2]

Riverine ecosystems have adapted to natural discharge variations across seasons. However, evidence suggesting that climate change has already impacted magnitudes of river flow seasonality is limited to local studies, mainly focusing on changes of mean or extreme flows. This study introduces the use of apportionment entropy as a robust measure to assess flow-volume nonuniformity across seasons, enabling a global analysis. We found that ~21% of long-term river gauging stations exhibit significant alterations in seasonal flow distributions, but two-thirds of these are unrelated to trends in annual mean discharge. By combining a data-driven runoff reconstruction with state-of-the-art hydrological simulations, we identified a discernible weakening of river flow seasonality in northern high latitudes (above 50°N), a phenomenon directly linked to anthropogenic climate forcing.

Anthropogenic climate warming, which could drive changes in the hydrological cycle, has received increasing attention (*1*). Water availability, a key concern, is directly related to ecosystem functions and societal interactions (*2*, *3*). However, human activities are altering river flow patterns worldwide, both directly through flow regulations and indirectly through land-use change and the impacts of anthropogenic climate change (ACC) on air temperature, precipitation, soil moisture, and snowmelt regimes (*4*–*6*). Consequently, more than two-thirds of the world's rivers have been altered even without considering the indirect impacts from ACC, which is characterized by human-induced alterations in greenhouse gases and aerosols (*7*).

River flow seasonality (RFS) plays a critical role in floods and droughts, threatening water security and freshwater biodiversity (*4*, *8*). For example, a substantial portion of the early meltwater from snowpack depletion may ultimately flow into oceans without being available for human use (*9*). In addition, weakening RFS (e.g., flood frequency reduction) can greatly simplify community-wide riparian plant networks (*10*, *11*). Riparian vegetation subsequently influences freshwater biota to make seasonal use of riparian areas and floodplains for feeding or breeding purposes (*12*).

Recent studies have shown a tendency for changes in RFS from timing or magnitude perspectives (*5*, *6*, *13*). However, these studies either lack global representativeness or fail to consider the impact of ACC explicitly. Nonetheless, there is growing evidence that ACC has influences on seasonal river flow, as indicated by climate and hydrological model simulations (*14*, *15*). Moreover, human-induced seasonal changes were detected in the western United States (*16*). However, the question of whether ACC is detectable in the magnitude of RFS at global scales remains unanswered, and it is challenging to transfer the evidence across regions, as river flow may vary locally because of atmospheric, oceanic, and terrestrial modulation (*17*).

In this study, we used in situ observations of monthly average river flow (*18*) from 10,120 gauging stations with either a minimum data length of 35 years or uncertainty-controlled shorter records from 1965 to 2014. In addition, we used recently published datasets of observation-based global gridded runoff (GRUN) reconstructed from data-driven models calibrated with observations to achieve global-scale coverage (*19*). Multimodel results from the Inter-Sectoral Impact Model Intercomparison Project phase 2b (ISIMIP2b) are presented for detecting and attributing observed changes to human influences on the climate system (*20*). To inform our global analysis of seasonal flow regimes, a generalized seasonality index was developed by using apportionment entropy (AE) (*21*). AE nonparametrically quantifies how evenly flow rates are distributed across months; high AE indicates a uniform distribution (low RFS), and low AE points to large month-to-month differences (high RFS). AE can be used to characterize changes in a hydroclimatological context because it is statistically well suited to the characteristics of highly variable flow regimes (*21*, *22*).

Changes in the trend of river flow seasonality

The northern high latitudes (above 50°N) showed discernible weakening in the seasonal cycle of river flow [increasing AE (fig. S1)] (Fig. 1). In northern North America (N. NA), ~40% of stations showed significantly decreasing RFS ($P < 0.05$). In comparison, only ~2% showed significantly increasing trends of RFS. Similar results were also observed in south Siberia (S with ~32% of stations showing significantly decreasing seasonality and only ~1% of stations showing significantly increasing seasonality. We further found a comparable pattern in Europe (EU), with ~19% of the stations experiencing significantly decreasing RFS, mainly located in northern Europe (N. EU), western Russia (W. RU), and the European Alps, whereas ~4% showed significantly increasing RFS, mainly concentrated downstream of the Alps (Fig. 1C). In addition, regions in the contiguous United States (CONUS) present predominantly decreasing trends of RFS overall, except for rivers in the Rocky Mountains and Florida in the western and eastern CONUS, respectively. In central North America (C. NA), significantly decreasing RFS trends account for ~18% of stations, in contrast with 4% that show significantly increasing RFS trends (Fig. 1D). W. RU, upper Midwest (U. Midwest), and S. SI display greater changes in magnitude for RFS trends. Although more than half of the stations in the northern high latitudes showed no statistically significant ($P > 0.05$) trends, both the significant and nonsignificant trends tell the same story, that is, RFS decreased in the northern high latitudes. Contrary to the above results, increasing RFS was observed in ~25% of the stations in southeast Brazil (S. BR) versus ~4% with decreasing RFS. Global patterns in seasonality trends during the more recent period of 1970 to 2019 generally agree with the trends computed for the 1965 to 2014 time frame (fig. S2). However, it should be noted that some spatial resolution was lost when we used the 1970 to 2019 time window, for example, in W. RU, because data are not available for a sufficient length of time.

Monthly high- and low-flow changes mediate seasonality

For better interpretation of seasonal variations, AE trends were combined with annual mean river flow trends (fig. S3A) to divide stations into six types (Fig. 2). For each station, we define low-flow months as the three calendar months with the lowest long-term monthly mean river flow, whereas high-flow months are the three calendar months with greatest monthly mean flow. Therefore, trends in low- and high-flow months (T_{LH}) contribute to annual mean and seasonal variations of river flow. We found seasonal variations in the northern high latitudes to be dominated by increasing low flows and decreasing high flows (L+H−; increasing trends of low flows and decreasing trends of high flows), accounting for ~46% of sites, and increasing low flows (L+H*; increasing trends of low flows and nonprominent changes in high flows) solely accounting for ~14%. These two patterns result in a significant decrease in RFS with no significant annual mean trends (L+H−) or significantly

---

[1] School of Environmental Science and Engineering, Southern University of Science and Technology, Shenzhen 518055, China. [2] water@leeds, School of Geography, University of Leeds, Leeds LS2 9JT, UK. [3] North China University of Water Resources and Electric Power, Zhengzhou 450046, China. [4] Henan Provincial Key Lab of Hydrosphere and Watershed Water Security, North China University of Water Resources and Electric Power, Zhengzhou 450046, China. [5] Institute for Atmospheric and Climate Science, ETH Zürich, 8092 Zürich, Switzerland.
*Corresponding author. Email: liujg@sustech.edu.cn

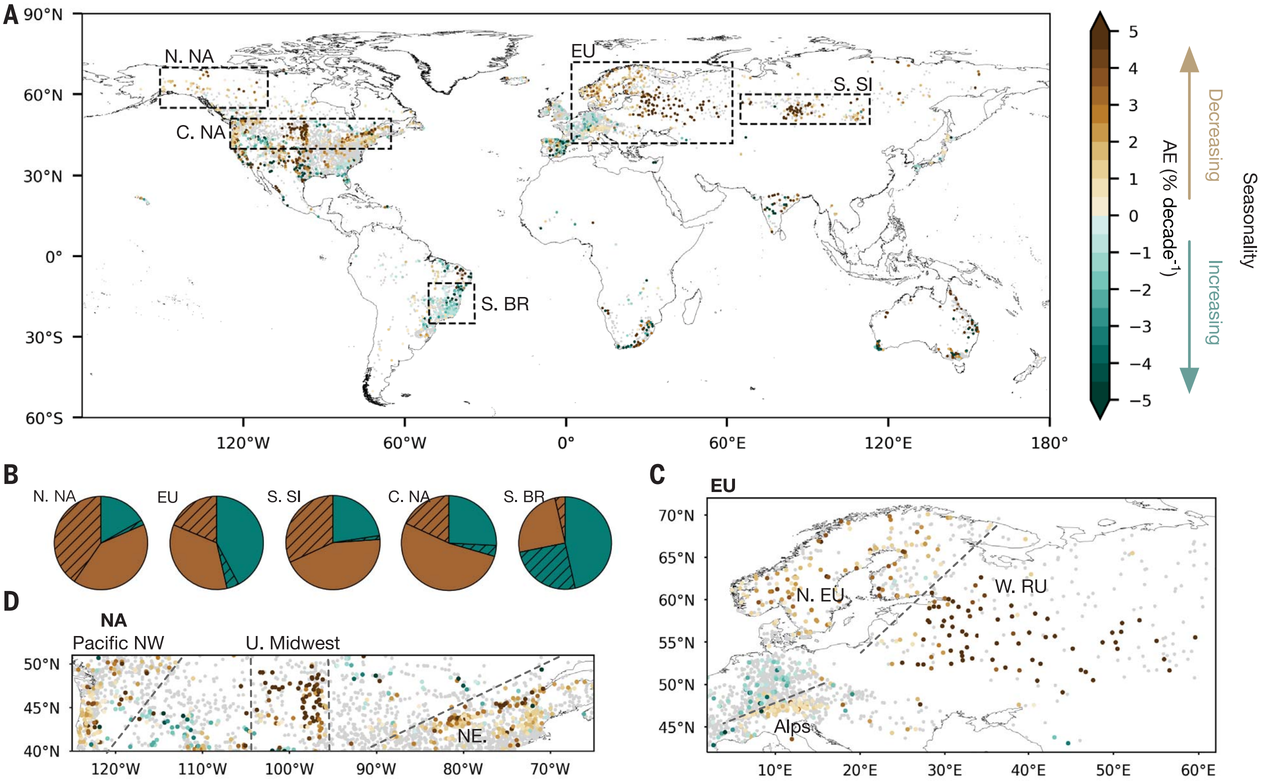

Fig. 1. RFS trends represented by AE (% decade^{-1}) over 50 years (1965 to 2014). (**A**) Map shows stations with significant RFS trends ($P < 0.05$); green represents increasing RFS and decreasing AE trends, and brown represents decreasing RFS and increasing AE trends. Stations with nonsignificant changes ($P > 0.05$) are represented by smaller gray dots. The five boxes mark the regions of interest: N. NA, EU, S. SI, C. NA, and S. BR. (**B**) Pie charts show the distribution of significant ($P < 0.05$, hatched) and nonsignificant ($P > 0.05$, solid) trends, corresponding to the direction of increasing (green) and decreasing (brown) RFS trends in five boxed regions. (**C** and **D**) Subareas in (C) EU and (D) C. NA that were dominated by the same AE change direction are delimited by dashed gray lines: N. EU, W. RU, the high-elevation European Alps, Pacific Northwest, upper Midwest, and northeast CONUS. Significance was estimated by the Mann-Kendal trend test.

increasing annual mean trends (L+H*). The distribution of the two patterns agrees with broad-scale climate trends in snowmelt-dominated regions (N. NA, N. EU, W. RU, S. SI, higher-elevation European Alps, U. Midwest, and northeast CONUS) (Fig. 2). Out of 1137 stations in the snowmelt-dominated areas (Fig. 2A, gray regions), 979 were experiencing significant weakening of RFS. Around 30% of river gauges displayed significantly increasing RFS and prominent low-flow decreases, herein represented as L−H* (~12%) and L−H+ (~18%), such as in Florida and the Rocky Mountains in the CONUS, lower catchments of the European Alps, and S. BR. A smaller number of sites experienced changes in high-flow months, including L*H+ (~2%) and L*H− (~8%), suggesting that high flows alone play a minor role in influencing RFS trends.

Overall, most stations showed L+H− and L−H+ (~65%), indicating that low and high flows interact to affect seasonality and mask annual mean trends of river flow (fig. S3B). Moreover, the proportion of sites (L−H* and L+H*; ~26%) where low-flow variations are the predominant factor is double that of high-flow variations (L*H+ and L*H−; ~9%), highlighting the key role that low-flow changes played in the AE shifts. Trends of annual low and high flows were analyzed separately (fig. S4), supporting our findings that increasing river flow in low-flow months is contributing to weakening RFS in the snowmelt-dominated areas.

Our results are consistent with those of other studies that have explored seasonal trends at regional scales. For example, earlier timing and reduced flood magnitude have been observed in N. EU, W. RU, and the European Alps (*5*, *6*). Previous studies also support findings of stations facing increasing RFS. For instance, the frequency of low-flow events increased in the low-flow season (*23*), corresponding to the spreading of L−H+ and L−H* categories. In the Rocky Mountains region (CONUS), early snowmelt can reduce river flow in low-flow months owing to less extensive spring snow cover (L−H*), which aligns with (*11*). Moreover, stations characterized by L−H+, such as those in S. BR, suggest a high risk of hazards from both drought and flood events, which aligns with (*24*, *25*).

Regional seasonality changes and potential mechanisms

To understand the change of RFS trends regionally, we focused on annual mean and monthly river flow trends and normalized flow regimes in nine hotspots (fig. S5). Increasing trends were most pronounced in low-flow months, except in S. BR, which was in agreement with a large proportion of L+H− and L+H* stations (Fig. 2). This suggests that the upper limit of the environmental flow envelopes is increasingly being exceeded during low-flow months in high latitudes (*26*). To interpret the potential mechanism of RFS trends, we chose subspaces of nine hotspots for a finer analysis (fig. S6). In snowmelt-dominated regions, decreasing snow fraction corresponding to snow-rain transition and snowpack depletion plays a more important role in shaping RFS than precipitation. Warmer temperatures can deplete snowpacks, contributing to greater frequency of high-flow events and lower frequency of low-flow events prior to the normal flood season, and hence reducing monthly differences in river flow (*5*, *23*). Early spring greening, closely related to early spring snowmelt,

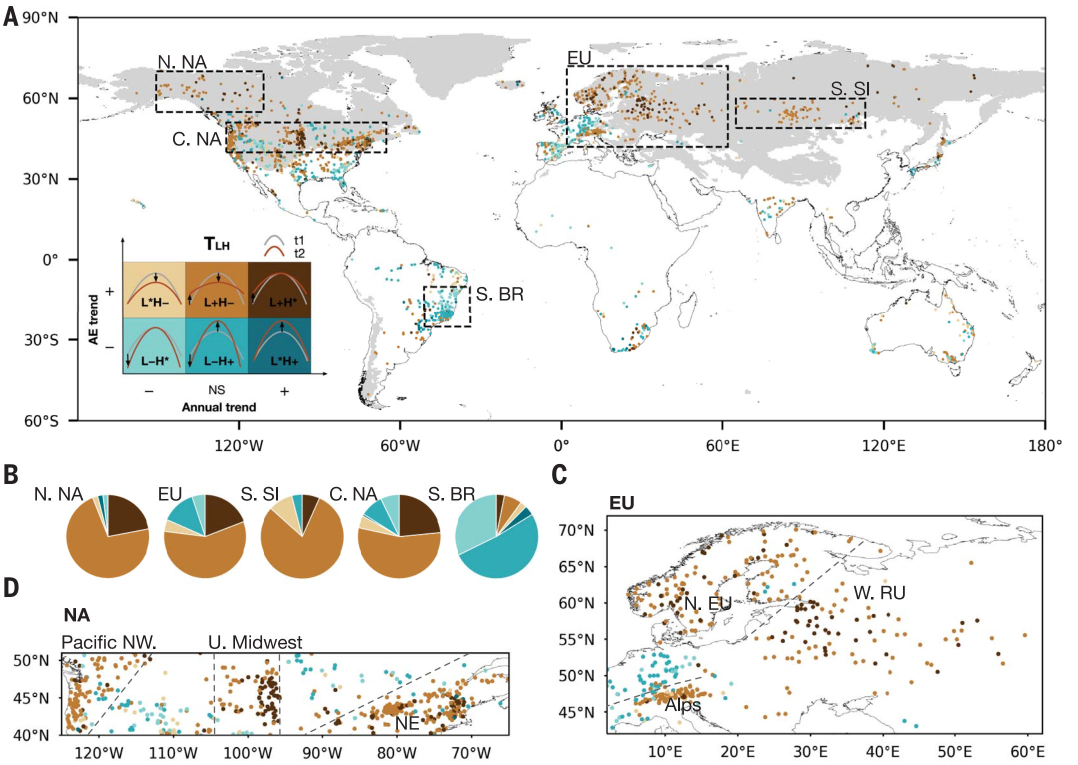

Fig. 2. Classification of potential reasons for changes in RFS. (**A**) Spatial distribution of T_{LH} indicated by change directions of AE and annual mean river flow (NS, not significant). *, no predominant changes of low or high flows. Labels show illustrations of flow-regime changes from period t1 to t2, corresponding to six types of T_{LH}. Regions where snow fraction in precipitation was >0.2 are shown in gray as snowmelt-dominated areas. The five boxes mark the regions of interest: N. NA, EU, S. SI, C. NA, and S. BR. (**B**) Pie charts show the proportion of T_{LH} in the five boxed regions in (A). (**C** and **D**) Subareas in (C) EU and (D) C. NA with the same AE change direction are delimited by dashed gray lines: N. EU, W. RU, the high-elevation European Alps, Pacific Northwest, upper Midwest, and northeast CONUS.

can exacerbate soil moisture deficits in spring and summer [high-flow months in snowmelt-dominated areas; e.g., the Alps (fig. S6)] (*27*). This can indirectly dampen river flow regimes by reducing runoff generation in high-flow months. However, decreasing RFS can also coincide with increasing soil moisture in high-flow months [e.g., W. RU (fig. S6)]. More precipitation falling as rain when air temperatures are around freezing is associated with shallower snowpacks and likely increased infiltration resulting from less frozen upper soil layers and therefore leads to a rise in soil moisture and smaller floods in the spring flood season (*5*). Soil moisture initially decreased before increasing in N. NA, northeast CONUS, and S. SI, indicating a shift of primary driving factor (fig. S6). Additionally, permafrost mass loss may continue to generate runoff thereafter [e.g., S. SI (fig. S5E)] (*28*).

Precipitation plays a more important role in RFS in non–snowmelt-dominated regions. For instance, seasonality of precipitation and river flow are positively correlated (table S1; Spearman rank correlation coefficients, $r = 0.65$) owing to the dominance of rain in the coast of the Pacific Northwest (fig. S6) (*23*). Similarly, increased RFS is associated with increased precipitation seasonality in S. BR (table S1; $r = 0.93$) (fig. S6), in agreement with (*29*). We noticed that most stations in the Pacific Northwest show increasing monthly river flow in the late spring and summer, contradicting the findings of previous studies (fig. S5F) (*4*, *30*). The reason for the difference between results may be due to varied El Niño Southern Oscillation (ENSO) impacts in different study periods (*31*). Temperature anomalies in ENSO phases strongly influence precipitation and snow accumulation and in turn affect spring and summer river flow.

Climate change detection and attribution analysis of RFS trends

To investigate whether ACC has caused the consistent decreasing trends of RFS in northern high latitudes, we augmented the assessment of in situ observations with an analysis of the GRUN to obtain a comprehensive spatial and temporal representation of RFS trends (*19*). The reconstructed spatial trend patterns of AE were compared with the corresponding trend pattern estimated by a multimodel ensemble mean of 27 simulations from global hydrological models (GHMs) (*20*). These GHMs considering human water and land use (HWLU) are driven by atmospheric data from climate models that account for historical radiative forcing (HIST) (scenario abbreviated as HIST&HWLU) (*20*). The simulated trends were consistent with the reconstruction, highlighting that the GHM simulations generally capture the observed changes (Fig. 3, A, B, and D). Simulations from GHMs also showed a general agreement above 50°N that supports the spatial pattern of RFS changes (fig. S7). Some differences are expected between the multimodel mean and observations. For example, the magnitude of AE trends was weaker in the multimodel mean. This weaker magnitude is most likely due to the averaging across the ensemble that reduces the effects of internal variability in the climate forcing, whereas the GRUN reconstruction represents a single observed evolution of the system (*32*). GRUN does not account for the effects of HWLU, which possibly caused some differences in the magnitude of AE trends. In addition, the high uncertainties of GRUN reconstruction and multimodel simulations possibly contribute to the disagreement in the Arctic region of northern Canada. However, the simulated trends in AE that are derived from GHMs that account for HWLU and are driven with atmospheric variables from preindustrial control climate models simulations (Picontrol&HWLU) failed to capture the observed changes (Fig. 3, C and D), indicating that HWLU is not contributing to the weakening pattern of RFS. Analyses from 1970 to 2019 showed the same trends in RFS, indicating that simulations are consistent with observations only when ACC is considered (figs. S8 and S9).

To quantitatively assess the influence of ACC on the observed spatial pattern and temporal evolution of RFS across northern high latitudes, correlation-based (*17*, *32*, *33*) and optimal fingerprinting methods (*17*, *33*, *34*) were used to test against the null hypothesis that there is no detectable pattern of AE trends in the observations resulting from ACC. The correlation approach uses all available AE trends and

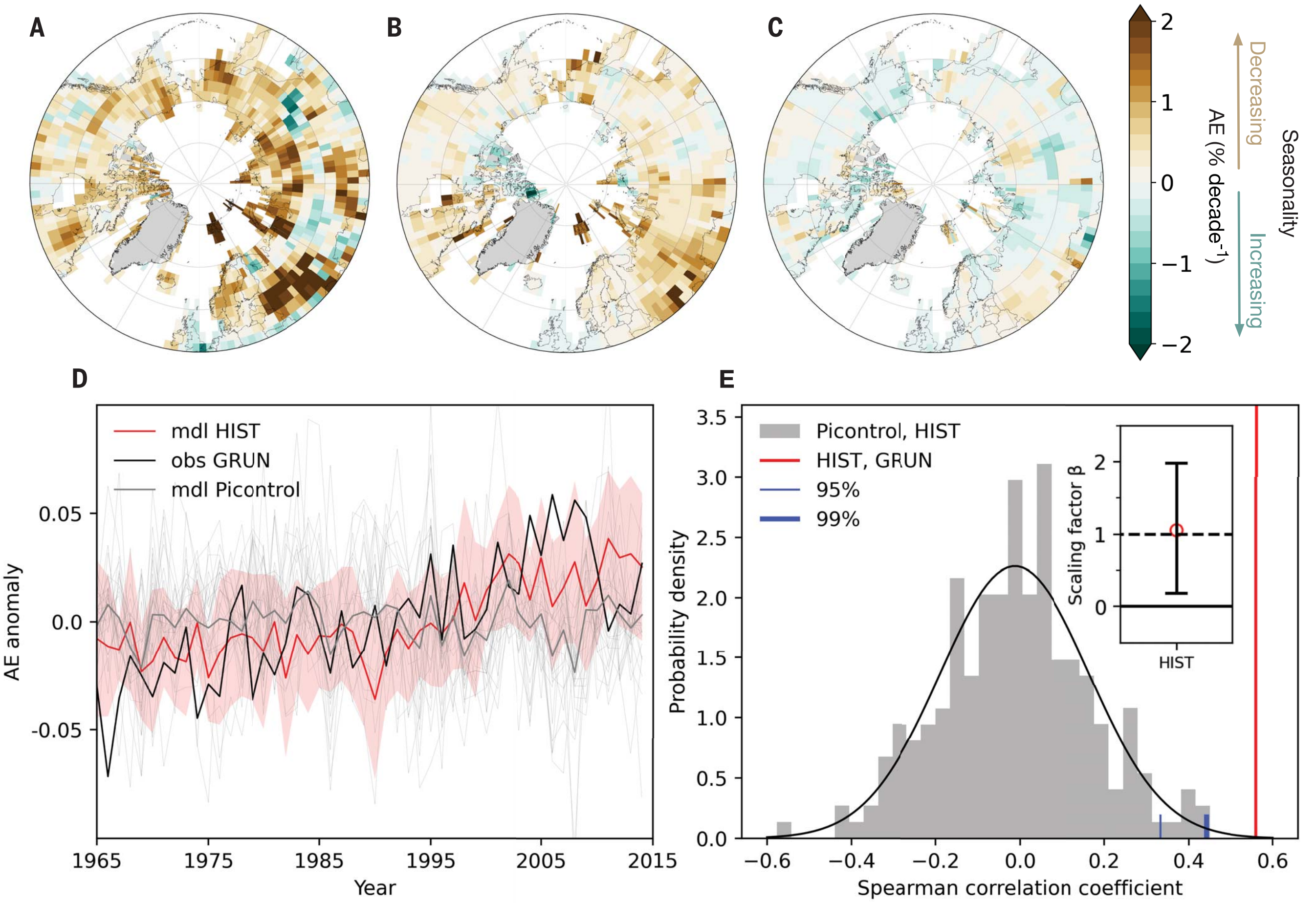

Fig. 3. Comparison of AE trends from observation-based reconstructions and global hydrological models for 1965 to 2014 (% decade^{-1}) in the northern high latitudes (above 50°N). (**A**) Reconstruction from GRUN. (**B** and **C**) Simulated changes based on the multimodel mean that account for HWLU under the effects of either HIST (B) or Picontrol (C). Areas with annual precipitation <100 mm and Greenland are masked in gray. (**D**) Multimodel (mdl) mean time series of annual AE anomalies for HIST&HWLU and Picontrol&HWLU responses and GRUN observations averaged for the northern high latitudes (above 50°N). The red spread is ensemble standard deviation of HIST&HWLU, and thin gray lines are 27-model results of Picontrol&HWLU. (**E**) Correlations of AE anomalies between simulations with and without ACC [corr$_{\text{temporary}}$(Picontrol, HIST)] or observation-based reconstruction [corr$_{\text{temporary}}$(HIST, GRUN)] across 50°N to 90°N. Spearman correlations between the multimodel mean from HIST&HWLU simulations and 216 chunks of Picontrol simulations with 50-year segments are shown as an empirical probability density function in gray. Vertical blue lines mark the 95 and 99% cumulative probabilities of an assumed normal distribution for the correlations. (Inset) The confidence interval of the scaling factor plot from optimal fingerprinting method with an uncertainty range of 0.5 to 99.5%. A signal was detected if the lower confidence bound was >0 (the solid line). The amplitude of the mean response was consistent with the observations if the confidence interval included 1 (the dashed line). The RCT passed (P > 0.1), indicating the consistency between the regression residuals and the model-simulated variability.

anomalies of simulations under HIST&HWLU and Picontrol (table S2). The spatial correlations between HIST simulations and a large ensemble of the Picontrol simulations were calculated from the multimodel simulation mean of AE trends forced with HIST and every chunk (216 estimates) of AE trends with Picontrol conditions (fig. S10). There was a 95% probability that the spatial Spearman correlations between multimodel mean of HIST simulations and GRUN [corr$_{\text{spatial}}$(HIST, GRUN)] were greater than what was expected from Picontrol simulations [corr$_{\text{spatial}}$(Picontrol, HIST]). This strongly suggests that ACC is the underlying cause for the spatial pattern of RFS. In addition, the temporal correlation of AE anomalies between multimodel mean of HIST simulations and GRUN [corr$_{\text{temporary}}$(HIST, GRUN)] was larger than for all correlations from Picontrol versus HIST [corr$_{\text{temporary}}$(Picontrol, HIST)] at 99% confidence level (Fig. 3E). These findings further confirm that human-induced emissions contribute to the decrease in RFS in the northern high latitudes.

An additional test used regularized optimal fingerprinting (*34*). Observations (y) are regressed on the multimodel mean of the simulation forced with HIST&HWLU (x) while considering sampling error v and natural variability derived from Picontrol&1860soc (ε): $y = \beta\,(x–v) + \varepsilon$. The inset in Fig. 3E displays the scaling factor β above zero at 99% confidence level in the experiment of HIST, suggesting that the simulations capture the observed AE changes when human-influenced climate changes are considered. Furthermore, the confidence interval of scaling factor β under HIST includes one, which implies that the magnitude of the simulated trend is consistent with the observations. Moreover, a residual consistency test (RCT) did not indicate an inconsistency between the regression residuals and the model-simulated variability (P > 0.1). An overall climate change detection and attribution analysis for 1970 to 2019 provided further evidence that human-induced emissions continue to contribute to decreased RFS in the northern high latitudes (fig. S11).

The primary climate change detection and attribution assessment that focuses on the northern high latitudes to optimize the signal-to-noise ratio is complemented with regional assessment (fig. S12). Changes of RFS were captured with 10 to 90% confidence intervals in Alaska, northern Europe, and northern Asia, defined by the Intergovernmental Panel on Climate Change Special Report on Extreme Events, only if ACC is considered. These results confirm the robustness of our conclusions regarding the influence of ACC on the temporal evolution of RFS in the northern high latitudes. Seasonality changes were also detected by model simulations that account for anthropogenic emissions in central America, southern Africa, and east Asia. This finding implies that human-induced emissions potentially exert an influence on the seasonality of monsoon precipitation and consequent runoff dynamics.

We acknowledge that human interference, such as flow regulation through reservoirs, may also contribute to RFS changes (*35*). Notably, however, more than three-fifths of the in situ observations, which are free from reservoir flow regulation (located in the subbasins with zero degree of regulation), exhibited the same spatial pattern of RFS trends as identified in our global dataset (fig. S13). Moreover, an observational reconstruction runoff derived from GRUN, which is free from human interference (including reservoirs, human water management, and land-use change), demonstrated a similar trend to that observed at the stations, though with smaller magnitudes of RFS trends (fig. S14). Additionally, simulations replicating preindustrial climate conditions but considering historical human activities (Picontrol&HWLU) failed to reproduce the trend of RFS in the northern high latitudes. Combining the climate change detection and attribution analysis for grid cells where direct observation data are available robustly showed that ACC contributes to the weakening of RFS in the northern high latitudes (fig. S15). We note that historical natural climate forcing (i.e., solar and volcanic activity) was not excluded when using ISIMIP2b to undertake the climate change detection and attribution analysis (*36*). Nonetheless, natural climate forcing has a limited impact on river flow owing to much smaller solar changes compared with ACC (*37*) and the short-lived influence of volcanic eruptions (*38*). Furthermore, no significant trends of precipitation seasonality have been observed in the northern high latitudes, demonstrating that precipitation seasonality change cannot account for our results (fig. S16). It is likely that observed rain-snow transition and increasing snowmelt under global warming led to a weakening trend of RFS in the northern high latitudes (fig. S6 and table S1). The underlying physics behind this assertion is temperature driven rather than precipitation driven, and ACC is acknowledged to far surpass natural forcing in dominating a warming future (*37*).

Our findings present changes in the seasonal cycles of river flow by adapting an AE perspective and clearly demonstrate that decreased RFS is attributable to ACC in the northern high latitudes. Possible climatic mechanisms that might drive flow-regime dampening under ACC include early snowpack depletion (*23*), loss of glacier extent (*39*), permafrost loss (*40*), increasing proportion of precipitation as rainfall (*41*), and shorter freezing periods (*42*, *43*) interacting with ocean-atmosphere oscillations (*31*). Depending on the region, some of these drivers can be more important than others in explaining RFS changes.

This study provides a standpoint for understanding changing seasonal patterns of river flow. There is an increasing need for accelerated climate adaptation efforts to safeguard freshwater ecosystems, achieved through, for example, use of managed environmental flows (*8*). Additionally, these efforts are essential for establishing sustainable water resource management by identifying and mitigating risks related to flood and drought, exploring seasonal storage opportunities, and optimizing allocations for irrigation or hydropower generation (*4*, *44*). It should be noted that water management might synergistically contribute to RFS dampening (*35*, *45*). Therefore, it is essential to develop mitigation strategies and adaptation planning to alleviate the future homogenization of seasonal river flow, particularly in locations such as European Russia, Scandinavia, and Canada.

REFERENCES AND NOTES

1. P. Wu, N. Christidis, P. Stott, *Nat. Clim. Chang.* **3**, 807–810 (2013).
2. C. J. Vörösmarty, P. Green, J. Salisbury, R. B. Lammers, *Science* **289**, 284–288 (2000).
3. P. C. D. Milly, K. A. Dunne, A. V. Vecchia, *Nature* **438**, 347–350 (2005).
4. N. K. Singh, N. B. Basu, *Nat. Sustain.* **5**, 397–405 (2022).
5. G. Blöschl *et al*., *Nature* **573**, 108–111 (2019).
6. G. Blöschl *et al*., *Science* **357**, 588–590 (2017).
7. M. Dynesius, C. Nilsson, *Science* **266**, 753–762 (1994).
8. M. Palmer, A. Ruhi, *Science* **365**, eaaw2087 (2019).
9. T. P. Barnett, J. C. Adam, D. P. Lettenmaier, *Nature* **438**, 303–309 (2005).
10. J. D. Tonkin, D. M. Merritt, J. D. Olden, L. V. Reynolds, D. A. Lytle, *Nat. Ecol. Evol.* **2**, 86–93 (2018).
11. S. B. Rood *et al*., *J. Hydrol. (Amst.)* **349**, 397–410 (2008).
12. H. L. Bateman, D. M. Merritt, *Glob. Ecol. Conserv.* **22**, e00957 (2020).
13. C. Wasko, R. Nathan, M. C. Peel, *Water Resour. Res.* **56**, e2020WR027233 (2020).
14. S. Eisner *et al*., *Clim. Change* **141**, 401–417 (2017).
15. K. Marvel *et al*., *Earths Futur.* **9**, e2021EF002019 (2021).
16. T. P. Barnett *et al*., *Science* **319**, 1080–1083 (2008).
17. L. Gudmundsson, S. I. Seneviratne, X. Zhang, *Nat. Clim. Chang.* **7**, 813–816 (2017).
18. H. X. Do, L. Gudmundsson, M. Leonard, S. Westra, *Earth Syst. Sci. Data* **10**, 765–785 (2018).
19. G. Ghiggi, V. Humphrey, S. I. Seneviratne, L. Gudmundsson, *Earth Syst. Sci. Data* **11**, 1655–1674 (2019).
20. K. Frieler *et al*., *Geosci. Model Dev.* **10**, 4321–4345 (2017).
21. X. Feng, A. Porporato, I. Rodriguez-Iturbe, *Nat. Clim. Chang.* **3**, 811–815 (2013).
22. G. Konapala, A. K. Mishra, Y. Wada, M. E. Mann, *Nat. Commun.* **11**, 3044 (2020).
23. E. N. Dethier, S. L. Sartain, C. E. Renshaw, F. J. Magilligan, *Sci. Adv.* **6**, eaba5939 (2020).
24. M. R. Viola, C. R. de Mello, S. C. Chou, S. N. Yanagi, J. L. Gomes, *Int. J. Climatol.* **35**, 1054–1068 (2015).
25. D. Bartiko, D. Y. Oliveira, N. B. Bonumá, P. L. B. Chaffe, *Hydrol. Sci. J.* **64**, 1071–1079 (2019).
26. V. Virkki *et al*., *Hydrol. Earth Syst. Sci.* **26**, 3315–3336 (2022).
27. X. Lian *et al*., *Sci. Adv.* **6**, eaax0255 (2020).
28. E. Gautier *et al*., *J. Hydrol. (Amst.)* **557**, 475–488 (2018).
29. V. B. P. Chagas, P. L. B. Chaffe, G. Blöschl, *Geophys. Res. Lett.* **49**, e2021GL096754 (2022).
30. P. W. Mote, S. Li, D. P. Lettenmaier, M. Xiao, R. Engel, *NPJ Clim. Atmos. Sci.* **1**, 2 (2018).
31. D. Lee, P. J. Ward, P. Block, *Environ. Res. Lett.* **13**, 044031 (2018).
32. R. S. Padrón *et al*., *Nat. Geosci.* **13**, 477–481 (2020).
33. L. Grant *et al*., *Nat. Geosci.* **14**, 849–854 (2021).
34. A. Ribes, S. Planton, L. Terray, *Clim. Dyn.* **41**, 2817–2836 (2013).
35. B. Arheimer, C. Donnelly, G. Lindström, *Nat. Commun.* **8**, 62 (2017).
36. L. Gudmundsson *et al*., *Science* **371**, 1159–1162 (2021).
37. IPCC, in *Climate Change 2013: The Physical Science Basis* (Cambridge Univ. Press, 2013), pp. 659–740.
38. C. E. Iles, G. C. Hegerl, *Nat. Geosci.* **8**, 838–842 (2015).
39. M. Huss, R. Hock, *Nat. Clim. Chang.* **8**, 135–140 (2018).
40. L. Gudmundsson, J. Kirchner, A. Gädeke, J. Noetzli, B. K. Biskaborn, *Environ. Res. Lett.* **17**, 095014 (2022).
41. W. R. Berghuijs, R. A. Woods, M. Hrachowitz, *Nat. Clim. Chang.* **4**, 583–586 (2014).
42. M. G. Floriancic, W. R. Berghuijs, P. Molnar, J. W. Kirchner, *Water Resour. Res.* **57**, e2019WR026928 (2021).
43. M. Mudelsee, M. Börngen, G. Tetzlaff, U. Grünewald, *Nature* **425**, 166–169 (2003).
44. J. D. Hunt *et al*., *Nat. Commun.* **11**, 947 (2020).
45. N. L. Poff, J. D. Olden, D. M. Merritt, D. M. Pepin, *Proc. Natl. Acad. Sci. U.S.A.* **104**, 5732–5737 (2007).
46. L. Gudmundsson, H. X. Do, M. Leonard, S. Westra, The Global Streamflow Indices and Metadata Archive (GSIM) - Part 2: Time Series Indices and Homogeneity Assessment, PANGAEA (2018); https://doi.org/10.1594/PANGAEA.887470.
47. G. Ghiggi, L. Gudmundsson, V. Humphrey, G-RUN: Global Runoff Reconstruction, Figshare, version 2, (2019); https://doi.org/10.6084/m9.figshare.9228176.v2.
48. U. Schneider, S. Hänsel, P. Finger, E. Rustemeier, M. Ziese, GPCC Full Data Monthly Product Version, 2022 at 2.5°: Monthly Land-Surface Precipitation from Rain-Gauges built on GTS-based and Historical Data, Deutscher Wetterdienst, (2022); https://doi.org/10.5676/DWD_GPCC/FD_M_V2022_250.
49. M. Cucchi *et al*., Near surface meteorological variables from 1979 to 2019 derived from bias-corrected reanalysis, Copernicus Climate Change Service (C3S) Climate Data Store (CDS), version 2.1, (2020); https://doi.org/10.24381/cds.20d54e34.
50. J. Muñoz Sabater, ERA5-Land hourly data from 1950 to present, Copernicus Climate Change Service (C3S) Climate Data Store (CDS), (2019); https://doi.org/10.24381/cds.68d2bb30.

ACKNOWLEDGMENTS

Funding: This study was supported by the National Natural Science Foundation of China (grant no. 42361144001), the Strategic Priority Research Program of the Chinese Academy of Sciences (grant no. XDA20060402), the Shenzhen Science and Technology Program (KCXFZ20201221173601003), the Henan Provincial Key Laboratory of Hydrosphere and Watershed Water Security, and the School of Geography and water@leeds at the University of Leeds. **Author contributions:** J.L., H.W., M.K., and J.H. conceived and designed the study. H.W. conducted the analyses and drafted the paper under the supervision of J.L., M.K., and J.H. All authors contributed to data interpretation and provided substantive revisions on the manuscript. **Competing interests:** The authors declare no competing interests. **Data availability:** The river flow time series from GSIM can be downloaded from https://doi.org/10.1594/PANGAEA.887470 (*46*). The runoff reconstruction dataset GRUN is available from

https://doi.org/10.6084/m9.figshare.9228176.v2 (*47*). The model results are available from the ISIMIP2b project in Water (global) sector (https://www.isimip.org/outputdata/). Other data are presented in the supplementary materials. The streamflow time series from the GRDC are available at https://www.bafg.de/GRDC. The observed monthly GPCC precipitation is available at https://doi.org/10.5676/DWD_GPCC/FD_M_V2022_250 (*48*). The CRUTEM5 dataset is available at https://www.metoffice.gov.uk/hadobs/crutem5/data/CRUTEM.5.0.1.0/download.html. The CPC soil moisture data can be downloaded from https://www.esrl.noaa.gov/psd. The bias-corrected reanalysis of WFDE5 and ERA5 monthly land data can be downloaded from the CDS website [WFDE5, https://doi.org/10.24381/cds.20d54e34 (*49*); ERA5, https://doi.org/10.24381/cds.68d2bb30 (*50*)].

SUPPLEMENTARY MATERIALS

science.org/doi/10.1126/science.adi9501
Materials and Methods
Figs. S1 to S18
Tables S1 to S3
References (*51*–*68*)

Submitted 28 May 2023; accepted 17 January 2024
10.1126/science.adi9501